POLITECNICO DI TORINO
Repository ISTITUZIONALE

A new lumped approach for the simulation of the magnetron injection gun for megawatt-class eu gyrotrons

(Article begins on next page)

11 April 2024

A second analysis to assess the suitability of the lumped approximation to the modeling of the emitter was carried out, focusing on the effect of the beam on the temperature distribution in the emitter. As already discussed above, when an accelerating voltage is applied to the emitter ring, the consequent emission of electrons causes a rapid cooling of its surface. This temperature variation then propagates inside the material, causing the appearance of a radial temperature distribution.

To evaluate the error caused by approximating this temperature distribution with the lumped parameter model, the heat equation is solved in a simplified model on a cylindrical computational domain approximating the emitter configuration, as shown in Figure 10. Thanks to the symmetry of the system, the z and θ components in the equation were discarded, leaving only the radial component to be evaluated.
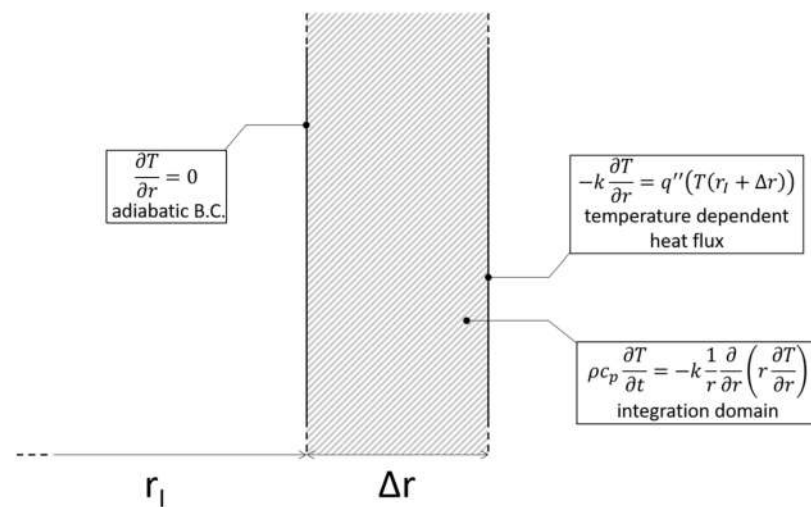

Figure 10. Solution domain for the simplified model for the evaluation of the suitability of the emitter-lumped model.

The integration domain is a simplification and schematization of the emitter thickness that will provide information on how the temperature wave propagates inside this component when the beam is turned on. On this domain, the material thermal conductivity is independent on time, position, and temperature.

The resulting problem for the simplified model is reported in Equation (4):

$$
\begin{cases}
\rho c_p \frac{\partial T}{\partial t} = -k\frac{1}{r}\frac{\partial}{\partial r}\left(r\frac{dT}{dr}\right) & \text{for } r \in [r_I, r_I + \Delta r], t \in \left(0, t_f\right] \\
T = T_0 & \text{for } r \in [r_I, r_I + \Delta r], t = 0 \\
\frac{\partial T}{\partial r} = 0 & \text{for } r = r_I, t \in \left(0, t_f\right] \\
-k\frac{\partial T}{\partial r} = q''\left(T(r)\right) & \text{for } r = r_I + \Delta r, t \in \left(0, t_f\right]
\end{cases}
\tag{4}
$$

where r_I is the radius of the internal surface of the emitter exposed to the filament, Δr is the thickness of the emitter ring measured from the internal surface to the emitting surface, and q'' represents the heat flux removed from this last one by the electron beam, and its magnitude is computed according to Equation (3).

Equation (4) was solved numerically by discretizing the spatial 1st and 2nd order derivatives according to central finite difference schemes. The time derivative was discretized using the Backwards Euler scheme to improve stability at the cost of added computational time.

In Figure 11 the numerical solution to the problem is shown from t = 0 s to t = 10 s with timesteps of 1s. As expected, the low temperature wave propagates inward, cooling down all the material.
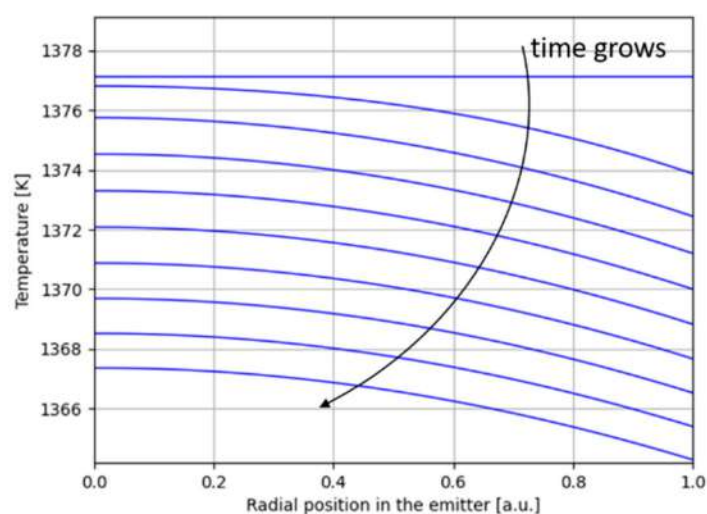
Figure 11. Radial distribution of the temperature computed in the simplified problem, as a function of the normalized radial position inside the emitter (the value 0 corresponds to the inner emitter surface, while value 1 corresponds to the outer surface, from which electrons are emitted).

For each timestep, the average temperature inside the emitter is computed, and then the percent deviation of the maximum and minimum temperatures are calculated. The results are shown in Figure 12. Figure 12a shows the results for the whole simulation time, while Figure 12b is a zoom to highlight the detail of the variation happening in the initial times. It can be noted that, even in the first instants of the evolution, the temperature distribution that results from the beam-cooling effect in the solid is quite uniform, with a maximum deviation from the average temperature of -0.167%. This can be ascribed to the fact that the emitter presents a small size and a high thermal conductivity.
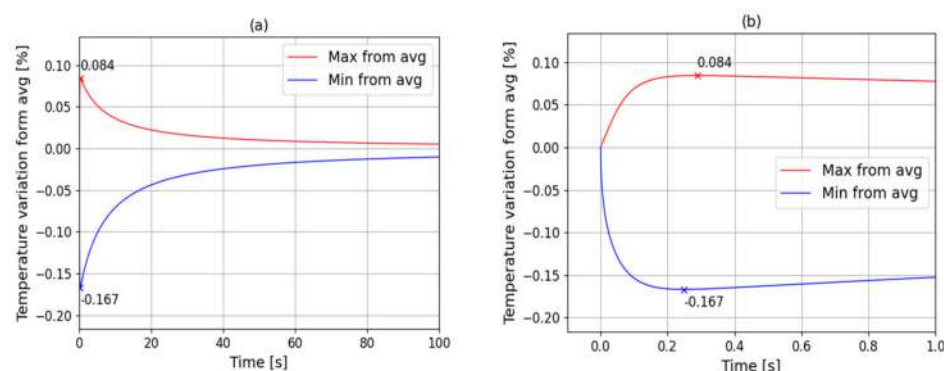

Figure 12. Percent deviation of maximum and minimum temperatures from average for the simplified model of the emitter. (**a**) Simulation for 100 s with 0.01 s timestep. (**b**) Simulation for 1 s with 0.0001 s timestep.

In view of the large temperature uniformity across the emitter, the analysis performed confirms the suitability of a lumped parameter approach, which subdivides the computational domain into a small number of regions described by a single temperature value, to model the thermal phenomena occurring inside the emitter ring with good precision. This happens because the temperature distributions in this object, generated both by the filament irradiation and by the beam cooling, are still quite uniform, thanks to the high thermal conductivity of the material and its reduced dimensions.

3.2. Implementation of the Lumped Model

Since the temperature of the exposed surface is the most important parameter that rules the intensity of the electron beam, the lumped model developed in the present

paper focuses on the emitter ring, subdividing it in a limited number of sub-zones. In Figure 13a, a vertical section of the emitter component is shown, subdivided into six sub-zones, following its natural geometry. Each sub-zone in the lumped model is considered to have a uniform temperature, which might be different from that of the adjacent sub-zones. The zones can transfer heat with the surroundings by conduction and radiation, undergoing the following three phenomena:

- Thermal diffusion through the emitter, modeled for two generic adjacent zones i and j, using geometrical thermal resistances, according to Equation (4):

$$R_{ij} = \frac{d}{kA_c} ln\left(\frac{r_2}{r_1}\right) \left[\frac{K}{W}\right] \tag{5}$$

  if the two masses are adjacent along the radial direction, and:

$$R_{ij} = \frac{d}{kA_c} \left[\frac{K}{W}\right] \tag{6}$$

  if they are adjacent in the vertical direction. Here, A_c is the contact area between two adjacent regions, and d is the distance between their barycenter.

- Radiative heat transfer to the surroundings, modeled for the generic mass i according to the following equation:

$$q_i'' = -K\sigma A_i \left(T_i^4 - T_{surr}^4\right) \left[\frac{W}{m^2}\right] \tag{7}$$

  where A_i is the area of the exposed area of zone i, σ is the Stefan–Boltzmann constant and K is a constant parameter calculated numerically, to keep into account the geometry of the surroundings.

- Electron emission and subsequent cooling effect modeled through the Richardson–Dushman equation, which applies only to the zone M4 and isdefined according to Equation (3).

A schematic of how the lumped zones interact with each other and their surroundings is shown in Figure 13b.

The lumped dynamical model simulating the propagation of heat inside the system and that calculates the temperature in the various zones was built, using Simulink®. The system has two inputs: the heating power applied to the heating element to rise the system temperature and the accelerating potential between anode and cathode. Note that the accelerating potential is used only to switch on and off the cooling term given by Equation (3), applied to the sub-zone #4, and to calculate the term ΔW according to Equation (2). The electric anode and cathode potentials can thus be considered as parameters of the system and are not of any interest for its dynamical behavior. The values used as input time series in the simulations are experimental values obtained at the Fusion for Energy FALCON facility, currently operational at EPFL Lausanne.
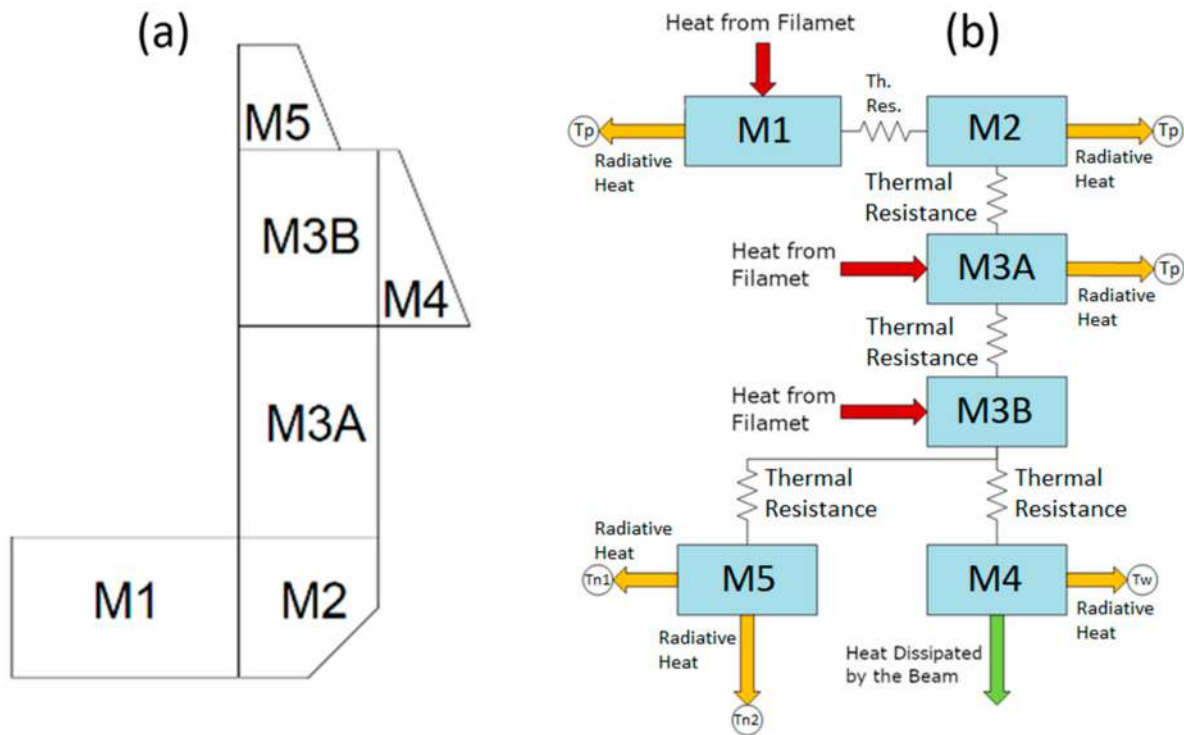
Figure 13. Scheme of the emitter ring sectioning (**a**) and of the models used to calculate heat transfer in the system (**b**). The radiative heat terms, thermal resistances, and beam heat are calculated according to Equations (5)–(7). Tn1 and Tn2 represent the average temperature of the nosecone seen by mass M5; Tw and Tp represent the average temperature of the MIG wall and of the prolongator.

4. Validation of the Model

To validate the model, different experimental shots obtained at the Fusion for Energy facility FALCON, at the EPFL premises in Lausanne [26–28] were used. The results calculated from Simulink were compared to the actual values of input current provided by the experiments. The values used as input time series in the simulations are experimental values of the input power and voltage. In Figures 14 and 15, two examples are shown where the lumped model proves to be able to behave as expected, calculating a current drop when the beam is turned on.

As we can see, even if the lumped model is extremely simplified and assumes the temperature to be uniform over wide regions of the emitter, the simulated current trend approximates the experimental data with relatively good precision. In Figure 15, for example, the error committed by the model is never higher than 2.5%; however, meanwhile, in Figure 14, it reaches up to almost 10%, where the spikes of the error are due to synchronization issues between the simulation data output and the experimental data. This variation in the precision of the model might be attributed to the fact that, when collecting data from experiments, each shot is recorded individually, and no information about the events that preceded its beginning is recorded. Thus, when comparing the result of the simulations to the actual experimental data, the initial state of the MIG's cathode might be different, for example, if another shot cooled down the emitter ring and not enough time was given to the system to return to the initial value considered in the simulation.
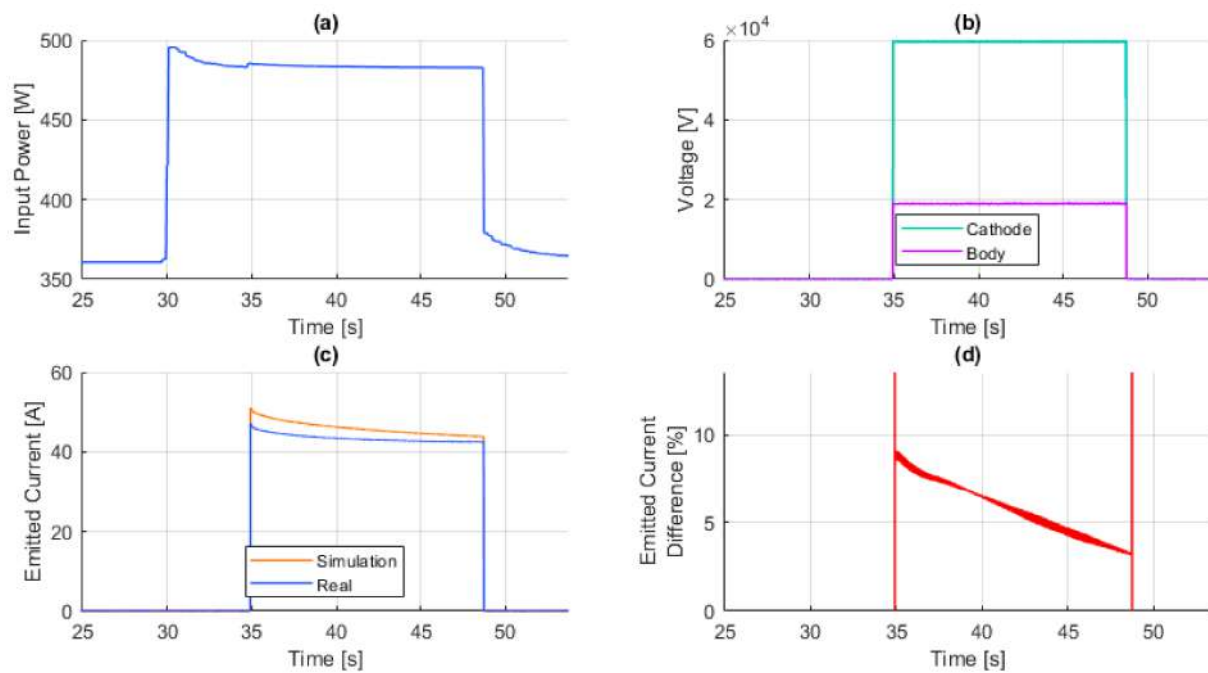
Figure 14. Shot 6679, comparison between the lumped model and experimental results: (**a**) input sequence of heating power, (**b**) input sequence of accelerating voltage, (**c**) comparison between the experimental and simulated time evolution of beam current, and (**d**) percentual error between the two.

Figure 15. Shot 6730, comparison between the lumped model and experimental results. (**a**) The input sequence of heating power, (**b**) input sequence of accelerating voltage, (**c**) comparison between the experimental and simulated time evolution of beam current, and (**d**) percentual error between the two.
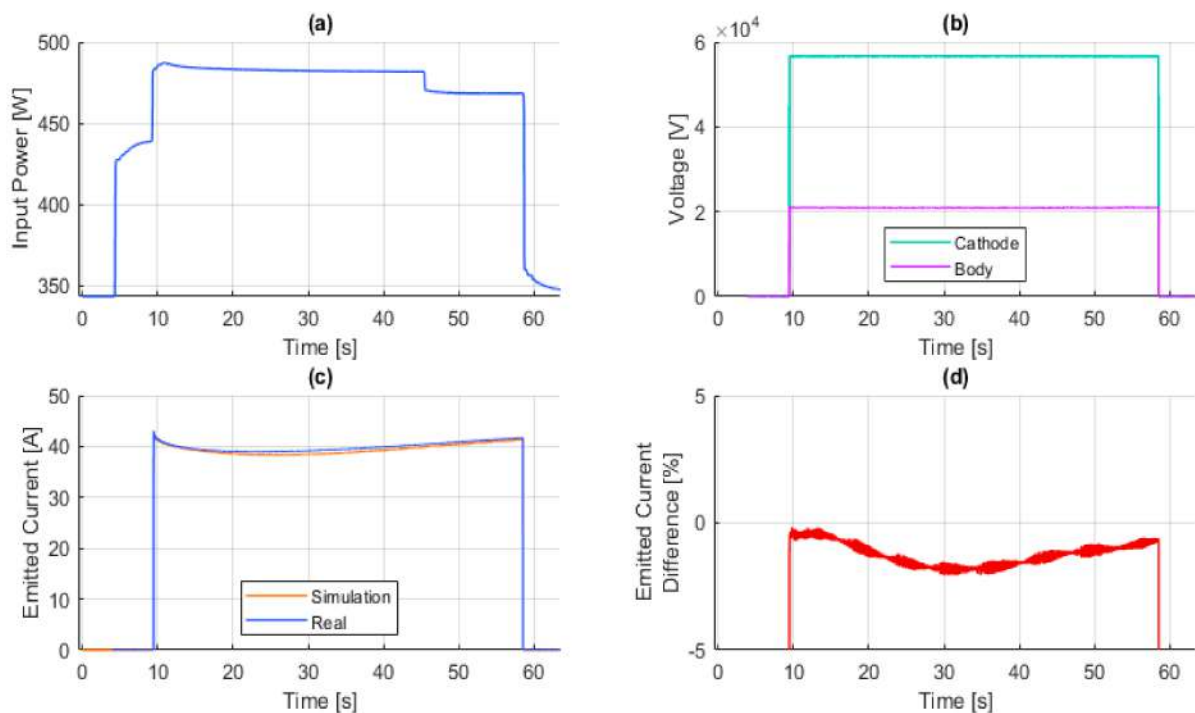
To better understand the performance of the lumped model, a deeper analysis of the error was carried out. A sample of 42 shots was considered, different in length, heating power profile, and accelerating voltage. For each of them, the Mean Absolute Percent Error

(MAPE) was calculated over the portion of time evolution in which the beam is on, and the results are shown in the histogram of Figure 16. From that, it can be deduced that, although the model performs well in simulating most of these shots, as shown by the high number of samples with a MAPE lower than 5%, there is a non-completely negligible number of samples whose MAPE is higher than this value. That might be due to the extreme variability of the experimental data available for the validation, and to the fact that some of the time sequences utilized were not acquired in perfectly reproducible conditions.
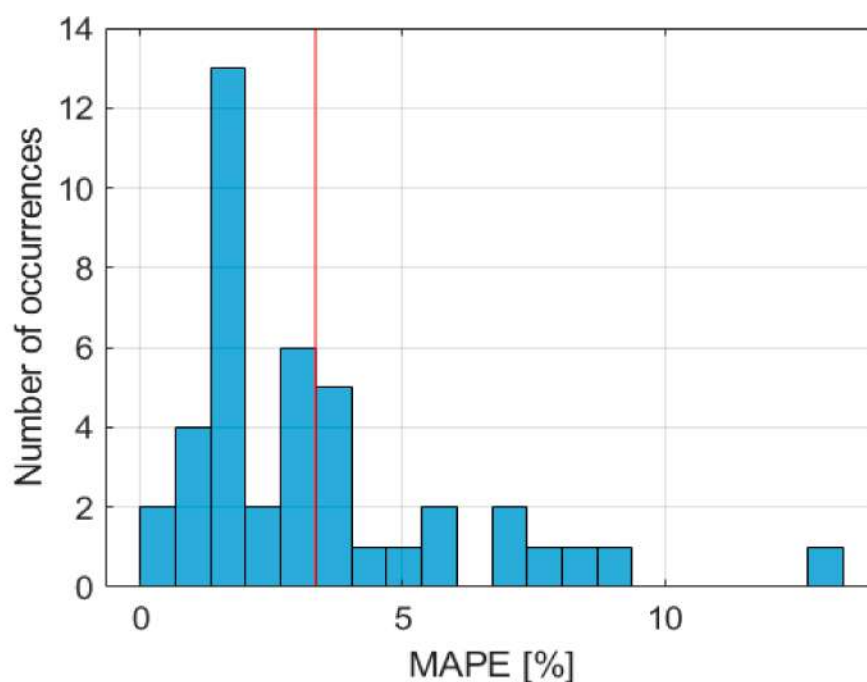

Figure 16. Distribution of the Mean Absolute Percent Error (MAPE) obtained by comparison between experimental data and simulations for 42 shots. The red line shows the average value of the MAPE.

Nevertheless, it must be pointed out that, even with its extreme simplicity, the model is able to reproduce the reality up to a precision level which is satisfying for the final purpose of this work, i.e., provide engineers a tool to simulate the system and test different configurations for possible control systems. Moreover, the simplicity of the model allows the simulation of long cathode operative times in a matter of seconds, and leaves space for future improvements, such as rising its complexity to achieve even better performance.

5. Conclusions

Due to the gap between the operative requirements and the actual behavior of the gyrotrons, a deep understanding of their dynamical behavior and the implementation of a control system is fundamental to ensure safe and stable operation of those machines during fusion related experiments.

In this work, the thermal behavior of the MIG's cathode was addressed by focusing on the physical phenomena involved in the beam generation. It has been shown that, in the European gyrotrons, the nominal temperature and electric fields force the system into the TL operative regime, where the beam current depends on the surface temperature of the emitter. This dependence, together with the cooling effect due to the electron extraction from the material, was addressed as the cause of the current drop observed during the long pulse experiments.

Having clarified the causes for the emitter current decay, the implementation of a lumped dynamical model, simulating the behavior of the cathode system, was performed. The aim of the model is to give the designer useful insights into the dynamical behavior of the system that can be used to predict the state of the gyrotron during its operation. To

do so, the model was built to be fast and precise. The lumped approach was justified a priori, by substantial and extended FEM analyses of the system, where the geometry was simulated by implementing radiation and conduction heat transfer. The detailed models showed a quite uniform temperature field, both during the electrical heating phase and beam-related cooling one, justifying the choice of a lumped parameter approach. The lumped model, implemented in Simulink®, takes as input the electrical power used to drive the heating elements needed to bring the system to the right temperature, and it computes in output the emitted current when the beam is on. The model was validated against experimental data, and a statistical error analysis was performed. The results show good agreement between the model predictions and the data, with the first being able to capture the dynamical behavior of the cathode. Moreover, the error analysis shows that, although a variability in the model precision is present, the mean average percent error remains below 5% in most of cases, with an average value of 3.34%. This behavior might be addressed to the variability on the experimental conditions from which the data were generated.

In the framework of further research on the operation of the European gyrotron, this model could be extremely useful both for the prediction of operational parameters and for the implementation of control systems. In a more general form, however, this model could be used either as a predictor of the state of the MIG, and as a starting point for a possible future implementation of a simulator of the whole gyrotron. That would require the analysis and the creation of other models to simulate different subsystems, for which several tools are already available [29–31]. Such a simulator could, at the end, allow for the development and testing of suitable controllers for the gyrotrons operation.

Author Contributions: Conceptualization, N.B., F.S., A.L. and A.C.; methodology, A.C. and L.S.; software, N.B.; validation, N.B., A.C. and F.S.; formal analysis, N.B. and F.S.; data curation, F.S. and A.L.; writing—original draft preparation, N.B.; writing—review and editing, A.C. and L.S.; visualization, N.B.; supervision, A.C. and L.S.; project administration, F.S. and A.L. All authors have read and agreed to the published version of the manuscript.

Institutional Review Board Statement: Not applicable.

Informed Consent Statement: Not applicable.

Data Availability Statement: Restrictions apply to the availability of these data. Data was obtained from Fusion for Energy and are available from the authors with the permission of Fusion for Energy.

Conflicts of Interest: The authors declare no conflict of interest.

References

1. Wesson, J.; Campbell, D.J. *Tokamaks*; Oxford University Press: Oxford, UK, 2011; Volume 149.
2. Organization, ITER Organization Website. Available online: https://www.iter.org/ (accessed on 5 October 2020).
3. Barabaschi, P.; Kamada, Y.; Shirai, H. Progress of the JT-60SA project. *Nucl. Fusion* **2019**, *59*, 112005. [CrossRef]
4. Wakatani, M. *Stellarator and Heliotron Devices*; Oxford University Press on Demand: Oxford, UK, 1998; Volume 95.
5. Wolf, R.C.; Alonso, A.; Äkäslompolo, S.; Baldzuhn, J.; Beurskens, M.; Beidler, C.D.; Biedermann, C.; Bosch, H.-S.; Bozhenkov, S.; Brakel, R.; et al. Performance of Wendelstein 7-X stellarator plasmas during the first divertor operation phase. *Phys. Plasmas* **2019**, *26*, 082504. [CrossRef]
6. Thumm, M.K.A.; Denisov, G.G.; Sakamoto, K.; Tran, M.Q. High-power gyrotrons for electron cyclotron heating and current drive. *Nucl. Fusion* **2019**, *59*, 073001. [CrossRef]

7.   Ioannidis, Z.C.; Albajar, F.; Alberti, S.; Avramidis, K.A.; Bin, W.; Bonicelli, T.; Bruschi, A.; Chelis, J.; Fanale, F.; Gantenbein, G.; et al. Recent experiments with the European 1MW, 170GHz industrial CW and short-pulse gyrotrons for ITER. *Fusion Eng. Des.* **2019**, *146*, 349–352. [CrossRef]

8.   Hogge, J.-P.; Albajar, F.; Alberti, S.; Avramidis, K.; Bin, W.; Bonicelli, T.; Braunmueller, F.; Bruschi, A.; Chelis, J.; Frigot, P.-E.; et al. Status and Experimental Results of the European 1 MW, 170 GHz Industrial CW Prototype Gyrotron for ITER. In Proceedings of the 2016 41st International Conference on Infrared, Millimeter, and Terahertz Waves (IRMMW-THz), Copenhagen, Denmark, 25–30 September 2016.

9.   Jelonnek, J.; Aiello, G.; Albaiar, F.; Alberti, S.; Avramidis, K.A.; Bertinetti, A.; Brucker, P.T.; Bruschi, A.; Chclis, I.; Dubray, J.; et al. From W7-X Towards ITER and Beyond: 2019 Status on EU Fusion Gyrotron Developments. In Proceedings of the 2019 International Vacuum Electronics Conference (IVEC), Busan, Korea, 28 April–1 May 2019.

10. Sakamoto, K.; Kajiwara, K.; Takahashi, K.; Oda, Y.; Kasugai, A.; Kobayashi, T.; Kobayashi, N.; Henderson, M.; Darbos, C. Development of High Power Gyrotron for ITER Application. In Proceedings of the 35th International Conference on Infrared, Millimeter, and Terahertz Waves, Rome, Italy, 5–10 September 2010.

11. Kasugai, A.; Minami, R.; Takahashi, K.; Kobayashi, N.; Sakamoto, K. Long pulse operation of 170GHz ITER gyrotron by beam current control. *Fusion Eng. Des.* **2006**, *81*, 2791–2796. [CrossRef]

12. Rozier, Y.; Albajar, F.; Alberti, S.; Avramidis, K.A.; Bonicelli, T.; Cismondi, F.; Frigot, P.-E.; Gantenbein, G.; Hermann, V.; Hogge, J.-P.; et al. Manufacturing and Tests of the European 1 MW, 170 GHz CW Gyrotron Prototype for ITER. In Proceedings of the 2016 IEEE International Vacuum Electronics Conference (IVEC), Monterey, CA, USA, 19–21 April 2016.

13. Idehara, T.; Kuleshov, A.; Ueda, K.; Khutoryan, E. Power-stabilization of high frequency gyrotrons using a double PID feedback control for applications to high power THz spectroscopy. *J. InfraredMillim. Terahertz Waves* **2014**, *35*, 159–168. [CrossRef]

14. Khutoryan, E.; Idehara, T.; Kuleshov, A.; Ueda, K. Gyrotron output power stabilization by PID feedback control of heater current and anode voltage. In Proceedings of the 2014 39th International Conference on Infrared, Millimeter, and Terahertz waves (IRMMW-THz), Tucson, AZ, USA, 14–19 September 2014.

15. Bakunin, V.L.; Denisov, G.G.; Novozhilova, Y.V. Frequency and phase stabilization of a multimode gyrotron with megawatt power by an external signal. *Tech. Phys. Lett.* **2014**, *40*, 382–385. [CrossRef]

16. Ogawa, I.; Idehara, T.; Ui, M.; Mitsudo, S.; Förster, W. Stabilization and modulation of the output power of submillimeter wave gyrotron. *Fusion Eng. Des.* **2001**, *53*, 571–576. [CrossRef]

17. Langmuir; Blodgett, K.B. Currents Limited by Space Charge between Coaxial Cylinders. *Phys. Rev.* **1923**, *22*, 347–356. [CrossRef]

18. Dushman, S. Thermionic Emission. *Rev. Mod. Phys.* **1930**, *2*, 381–476. [CrossRef]

19. Cronin, J.L. Modern Dispenser Cathodes. *IEEE Proc.* **1981**, *128*, 19–32. [CrossRef]

20. Petrin, B. Thermionic field emission of electrons from metals and explosive electron emission from micropoints. *J. Exp. Theor. Phys.* **2009**, *109*, 314–321. [CrossRef]

21. Charbonnier, F.M.; Strayer, R.W.; Swanson, L.W.; Martin, E.E. Nottingham Effect in Field and T—F Emission: Heating and Cooling Domains, and Inversion Temperature. *Phys. Rev. Lett.* **1964**, *13*, 397–401. [CrossRef]

22. OpenCFD Ltd. OpenFOAM®-Official Home of The Open Source Computational Fluid Dynamics (CFD) Toolbox. 2019. Available online: https://openfoam.com/ (accessed on 20 October 2020).

23. Siegel, R.; Howell, J.R.; Menguc, M.P. *Thermal Radiation Heat Transfer*, 5th ed.; CRC Press: Boca Raton, FL, USA, 2010.

24. OpenCFD Ltd. OpenFOAM API Guide: FvDOM Class Reference. 2019. Available online: https://www.openfoam.com/documentation/guides/latest/api/classFoam_1_1radiation_1_1fvDOM.html (accessed on 20 October 2020).

25. OpenCFD Ltd. OpenFOAM: Manual Pages: CheckMesh. OpenCFD Ltd. Available online: https://www.openfoam.com/documentation/guides/latest/man/checkMesh.html (accessed on 11 November 2020).

26. Ioannidis, Z.C.; Rzesnicki, T.; Albajar, F.; Alberti, S.; Avramidis, K.A.; Bin, W.; Bonicelli, T.; Bruschi, A.; Chelis, I.; Frigot, P.-E.; et al. CW experiments with the EU 1-MW, 170-GHz industrial prototype gyrotron for ITER at KIT. *IEEE Trans. Electron. Devices* **2017**, *64*, 3885–3892. [CrossRef]

27. Bonicelli, T.; Alberti, S.; Cirant, S.; Dormicchi, O.; Fasel, D.; Hogge, J.P.; Illy, S.; Jin, J.; Lievin, C.; Mondino, P.L.; et al. EC power sources: European technological developments towards ITER. *Fusion Eng. Des.* **2007**, *82*, 619–626. [CrossRef]

28. Rzesnicki, T.; Albajar, F.; Alberti, S.; Avramidis, K.A.; Bin, W.; Bonicelli, T.; Braunmueller, F.; Bruschi, A.; Chelis, J.; Frigot, P.-E.; et al. Experimental verification of the European 1 MW, 170 GHz industrial CW prototype gyrotron for ITER. *Fusion Eng. Des.* **2017**, *123*, 490–494. [CrossRef]

29. Avramides, K.A.; Pagonakis, I.G.; Iatrou, C.T.; Vomvoridis, J.L. EURIDICE: A code-package for gyrotron interaction simulations and cavity design. *Epj Web Conf.* **2012**, *32*, 04016. [CrossRef]

30. Bertinetti, A.; Albajar, F.; Avramidis, K.A.; Cau, F.; Cismondi, F.; Gantenbein, G.; Jelonnek, J.; Kalaria, P.C.; Ruess, S.; Rzesnicki, T.; et al. Analysis of an actively-cooled coaxial cavity in a 170 GHz 2 MW gyrotron using the multi-physics computational tool MUCCA. *Fusion Eng. Des.* **2019**, *146*, 74–77. [CrossRef]

31. Braunmueller, F.; Tran, T.M.; Vuillemin, Q.; Alberti, S.; Genoud, J.; Hogge, J.-P.; Tran, M.Q. TWANG-PIC, a novel gyro-averaged one-dimensional particle-in-cell code for interpretation of gyrotron experiments. *Phys. Plasmas* **2015**, *22*, 063115. [CrossRef]